Theoretical Investigations of Para-Methoxystyrene/Styrene Polymerization Catalyzed by Cationic Methyl- and Dibenzobarrelene-Based α-Diimine Palladium Complexes

Ling Zhu , Yi Luo * , Xin Wen , Wenzhen Zhang , Guangli Zhou *

Posted Date: 29 October 2024

doi: 10.20944/preprints202410.2300.v1

Keywords: Para-Methoxystyrene/Styrene Polymerization

Article

Theoretical Investigations of *para*-Methoxystyrene/Styrene Polymerization Catalyzed by Cationic Methyl- And Dibenzobarrelene-Based *A*-Diimine Palladium Complexes

Ling Zhu [1], Yi Luo [1,3,*], Xin Wen [1], Wenzhen Zhang [1], and Guangli Zhou [2,*]

[1] State Key Laboratory of Fine Chemicals, School of Chemical Engineering, Dalian University of Technology, Dalian 116024, China
[2] School of Chemistry and Chemical Engineering, Linyi University, Linyi 276000, China
[3] PetroChina Petrochemical Research Institute, Beijing, 102206, China
* Correspondence: luoyi010@petrochina.com.cn (Y.L.); zhouguangli@lyu.edu.cn (G.Z.)

Abstract: The polymerization mechanism of *para*-methoxystyrene catalyzed by cationic α-diimine palladium complexes with various ancillary ligands was rigorously examined using density functional theory. In the classical methyl-based α-diimine palladium complex [{(2,6-^{i}Pr$_2$C$_6$H$_3$)-N=C(Me)-C(Me)=N-2,6-^{i}Pr$_2$C$_6$H$_3$)}PdMe]$^+$ (**A**$^+$), the 2,1-insertion of *para*-methoxystyrene is favored over the 1,2-insertion, both thermodynamically and kinetically, during the chain initiation step. The resulting thermodynamically favored η^3-π-benzyl intermediates face a substantial energy barrier, yielding only trace amounts of polymer, as experimentally verified. In contrast, the dibenzobarrelene-based α-diimine palladium complex [{(2,6-^{i}Pr$_2$C$_6$H$_3$)-N=C(R)-C(R)=N-2,6-^{i}Pr$_2$C$_6$H$_3$)}PdMe]$^+$ (R = dibenzobarrelene, **B**$^+$) shows similar energy barriers for both 2,1- and 1,2-insertions. Continuous 2,1/2,1 or 2,1/1,2 insertions are impeded by excessive energy barriers. However, theoretical calculations reveal that the 1,2-insertion product can seamlessly transition into the chain propagation stage, producing a polymer with high 1,2-regioselectivity. The observed activity of complexes **A**$^+$ or **B**$^+$ towards *para*-methoxystyrene polymerization stems from the energy barrier differences between the 1,2- and 2,1-insertions, influenced by the steric hindrance from the ancillary ligands. Further investigation into the effects of steric hindrance on the chain initiation stage involved computational modeling of analogous complexes with increased steric bulk. These studies established a direct correlation between the energy barrier difference $\Delta\Delta G$ (1,2–2,1) and the van der Waals volume of the ancillary ligand. Larger van der Waals volumes correspond to reduced energy barrier differences, thus enhancing the regioselectivity for *para*-methoxystyrene polymerization. Moreover, the experimental inertness of complex **B**$^+$ towards styrene polymerization is attributed to the formation of stable kinetic and thermodynamic 2,1-insertion intermediates, which obstruct further styrene monomer insertion due to an extremely high reactive energy barrier. These findings contribute to a deeper understanding of the mechanistic aspects and offer insights for designing new transition metal catalysts for the polymerization of *para*-alkoxystyrenes.

Keywords: keyword 1; keyword 2; keyword 3 (List three to ten pertinent keywords specific to the article; yet reasonably common within the subject discipline.)

 doi:10.20944/preprints202410.2300.v1

1. Introduction

Functionalized polyolefins, which incorporate polar functional groups into polyolefins, represent a promising class of materials due to their distinctive properties such as wettability, adhesion, printability, and compatibility. These properties significantly expand their potential applications. [1–3] The successful introduction of polar functional groups into polyolefins has been achieved through various polymerization techniques including cationic polymerization [4,5], radical polymerization [6,7], and coordination-insertion polymerization. [8–11] Among these, coordination-insertion polymerization, facilitated by transition metal catalysts, has proven to be an efficient and straightforward method. This technique offers mild reaction conditions and allows precise control over the polymer's structure and composition.

Early transition metal catalysts, including group 4-6 metals, are susceptible to poisoning due to their strong Lewis acidity, which facilitates the easy coordination of polar monomers. [12–14] In contrast, late transition metal catalysts, such as square planar d^8 nickel and palladium complexes, exhibit low oxophilicity and enhanced tolerance to functional groups, making them ideal for synthesizing functionalized polyolefins. Over the past decades, the development of late-transition-metal catalysts for polar monomer polymerization has garnered significant interest in functional polyolefin research. [15–18] For instance, Mecking in 2009 first demonstrated the continuous insertion of methyl acrylate using a neutral phosphinesulfonato palladium(II) catalyst, achieving only trace amounts of oligomers. [19] Subsequently, the same group explored the polymerization behavior of diallyl ether catalyzed by identical palladium(II) complexes. [20] This catalyst displayed moderate catalytic activity for diallyl ether polymerization. Conversely, the homopolymerization of allyl ethyl ether resulted in products with significantly lower molecular weights and reduced productivity. The Pellecchia group developed a series of Ni(II) complexes with pyridylimino ligands, demonstrating high productivity but lower selectivity in methyl acrylate insertion for the copolymerization of ethylene with methyl acrylate. [21] However, the overall activity, selectivity, and insertion rates of polar monomers in these polymerization processes remain generally low, making it challenging to achieve the desired high molecular weights and high rates of polar monomer insertion.

Recently, considerable efforts have been invested in enhancing the polymerization performance of metal catalysts through modifications to ligand backbones, substituents, and metal centers. While some experimental instances have demonstrated success, a general lack of theoretical understanding concerning the regulation of catalytic activity, polymer molecular weight, and polar monomer insertion rates by late-transition metals often leads to inefficiency and a measure of trial-and-error in research. Consequently, it is essential to investigate the influence of the ligand backbone, substituents, and metal centers within metal complexes on polymerization activity at the molecular level.

In 2020, Gao and colleagues reported that the classical α-diimine palladium complex **A** catalyzed the polymerization of *para*-methoxystyrene (*p*MOS), yielding only trace amounts of the product. In contrast, the dibenzobarrelene-based α-diimine palladium species **B** demonstrated high activity, rapidly producing poly(*para*-methoxystyrene)s with high molecular weights. However, this catalyst **B** was inert when used for the polymerization of styrene (Scheme 1). [22] This observation underscores the significant influence of the auxiliary ligands and the type of monomer on the catalytic activity and microstructure of the polymerization process. Consequently, this study systematically investigates the mechanisms and origins of the activity in the polymerization of *p*MOS by late transition metal palladium complexes with varying auxiliary ligands. Additionally, it examines the monomer specificity of dibenzobarrelene-based α-diimine palladium species using density functional theory (DFT) calculations. These investigations aim to provide a theoretical foundation for designing and synthesizing new catalytic systems.

Preprints.org (www.preprints.org) | NOT PEER-REVIEWED | Posted: 29 October 2024 doi:10.20944/preprints202410.2300.v1

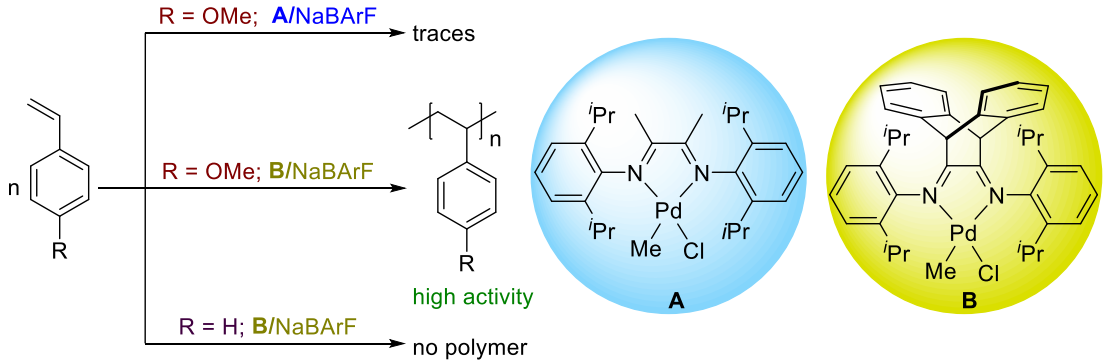

Scheme 1. Polymerization of *para*-methoxystyrene/styrene catalyzed by palladium complexes.

2. Results and Discussion

2.1. Mechanism of pMOS Polymerization by Cationic Species A⁺

The cationic palladium alkyl species **A⁺** was synthesized by reacting Pd–Cl with sodium tetrakis(3,5-bis(trifluoromethyl)phenyl)borate NaBArF from complex **A**. As depicted in Figure 1, the chain initiation and propagation processes of *p*MOS polymerization, catalyzed by the *α*-diimine palladium complex **A⁺**, were modeled using DFT calculations. The chain initiation can proceed via two pathways: 1,2- (black line) and 2,1- (green line) insertion of *p*MOS. In the 1,2-insertion, coordination of the C=C bond of *p*MOS with the palladium species **A⁺** leads to the formation of the stable 1,2-coordination complex ^{A}**1**$_{p\text{MOS12}}$ (ΔG = -11.6 kcal/mol). This is followed by the insertion of the C=C bond of *p*MOS into the Pd–C bond via the four-center transition state ^{A}**TS1**$_{p\text{MOS12}}$, requiring an energy barrier of 20.8 kcal/mol (8.3–(-12.5)) and resulting in an exothermic reaction of 17.4 kcal/mol, forming the intermediate ^{A}**3**$_{p\text{MOS12}}$. Conversely, in the 2,1-insertion, *p*MOS π-coordinates with species **A⁺** to form the 2,1-coordination complex ^{A}**1**$_{p\text{MOS21}}$. This complex then undergoes insertion via the four-center transition state ^{A}**TS1**$_{p\text{MOS21}}$, forming the complex ^{A}**2**$_{p\text{MOS21}}$ which exists with an agnostic interaction, then it subsequently transforms into a more stable π-η^3-benzyl chelate intermediate ^{A}**3**$_{p\text{MOS21}}$. The 2,1-insertion process has a lower free energy barrier of 18.0 kcal/mol (5.5–(-12.5)), which is 2.8 kcal/mol less than the 1,2-insertion. Additionally, the chain initiation product ^{A}**3**$_{p\text{MOS21}}$, resulting from the 2,1-insertion, releases 29.8 kcal/mol of energy, making it thermodynamically more stable than ^{A}**3**$_{p\text{MOS12}}$ by 12.4 kcal/mol. These calculations indicate that the 2,1-insertion mode is more favorable than the 1,2-insertion mode, both kinetically and thermodynamically, at the chain initiation stage. Thus, the subsequent chain propagation process was modeled based on the 2,1-insertion product ^{A}**3**$_{p\text{MOS21}}$.

During the chain propagation stage, both 1,2- and 2,1-insertion modes of *p*MOS were examined. The coordination of *p*MOS with the intermediate ^{A}**3**$_{p\text{MOS21}}$ to form ^{A}**4**$_{p\text{MOS12}}$ and ^{A}**4**$_{p\text{MOS21}}$ is endergonic, with energy increases of 10.9 and 12.9 kcal/mol respectively. Furthermore, the energy barrier for the 1,2-insertion, as modeled by the transition state ^{A}**TS2**$_{p\text{MOS12}}$, was calculated to be notably high at 33.1 kcal/mol. Similarly, the transition state for the 2,1-insertion, ^{A}**TS2**$_{p\text{MOS21}}$, also exhibited a significant energy barrier of 29.9 kcal/mol. These calculated free energy barriers for the chain propagation pathways are prohibitively high, considering the experimental reaction conditions at 30 °C, aligning with the observed trace amounts of polymer produced under these conditions.

Preprints.org (www.preprints.org) | NOT PEER-REVIEWED | Posted: 29 October 2024 doi:10.20944/preprints202410.2300.v1

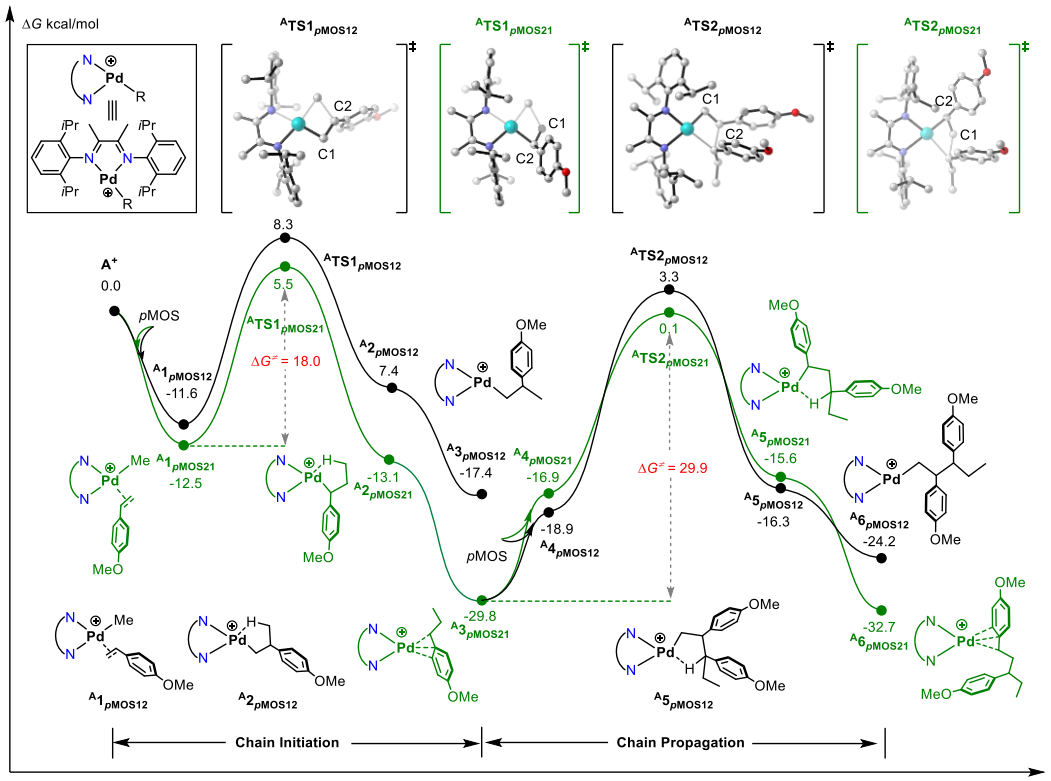

Figure 1. Calculated Gibbs free energy profiles for insertion of *p*MOS based on **A**⁺ at the chain initiation and chain propagation stage (in kcal/mol). The 1,2- and 2,1-insertion pathways are in black and green, respectively.

2.2. Mechanism of pMOS Polymerization by Cationic Species B⁺

Unlike the class *α*-diimine palladium catalyst **A**⁺, where only a trace amount of polymer was observed, the dibenzobarrelene-based *α*-diimine complex **B**⁺ demonstrated high activity in *p*MOS polymerization. To elucidate this intriguing reactivity difference, detailed mechanistic studies were undertaken. As with species **A**⁺, the chain initiation stage for *p*MOS polymerization based on complex **B**⁺ was calculated for both 2,1-insertion and 1,2-insertion pathways. As illustrated in Figure 2, the 2,1-insertion pathway ($^{B}\mathbf{1}_{p\text{MOS21}}\rightarrow{}^{B}\mathbf{TS1}_{p\text{MOS21}}\rightarrow{}^{B}\mathbf{2}_{p\text{MOS21}}\rightarrow{}^{B}\mathbf{3}_{p\text{MOS21}}$) involves an energy barrier of 21.3 kcal/mol and is accompanied by an exothermic release of 28.0 kcal/mol. Conversely, the 1,2-insertion pathway ($^{B}\mathbf{1}_{p\text{MOS12}}\rightarrow{}^{B}\mathbf{TS1}_{p\text{MOS12}}\rightarrow{}^{B}\mathbf{2}_{p\text{MOS12}}\rightarrow{}^{B}\mathbf{3}_{p\text{MOS12}}$) presents a relative free energy barrier of 20.9 kcal/mol and an exothermic release of 15.1 kcal/mol. Notably, the energy barrier gap (ΔΔG (1,2–2,1) between the 1,2- and 2,1-insertions shifted from 2.8 to -0.4 kcal/mol compared to **A**⁺. It is significant to note that the formation of intermediate $^{B}\mathbf{3}_{p\text{MOS12}}$ is exothermic by 15.1 kcal/mol, whereas intermediate $^{B}\mathbf{3}_{p\text{MOS21}}$ is exothermic by 28.0 kcal/mol, which is 12.9 kcal/mol more exothermic than the 1,2-insertion.

 doi:10.20944/preprints202410.2300.v1

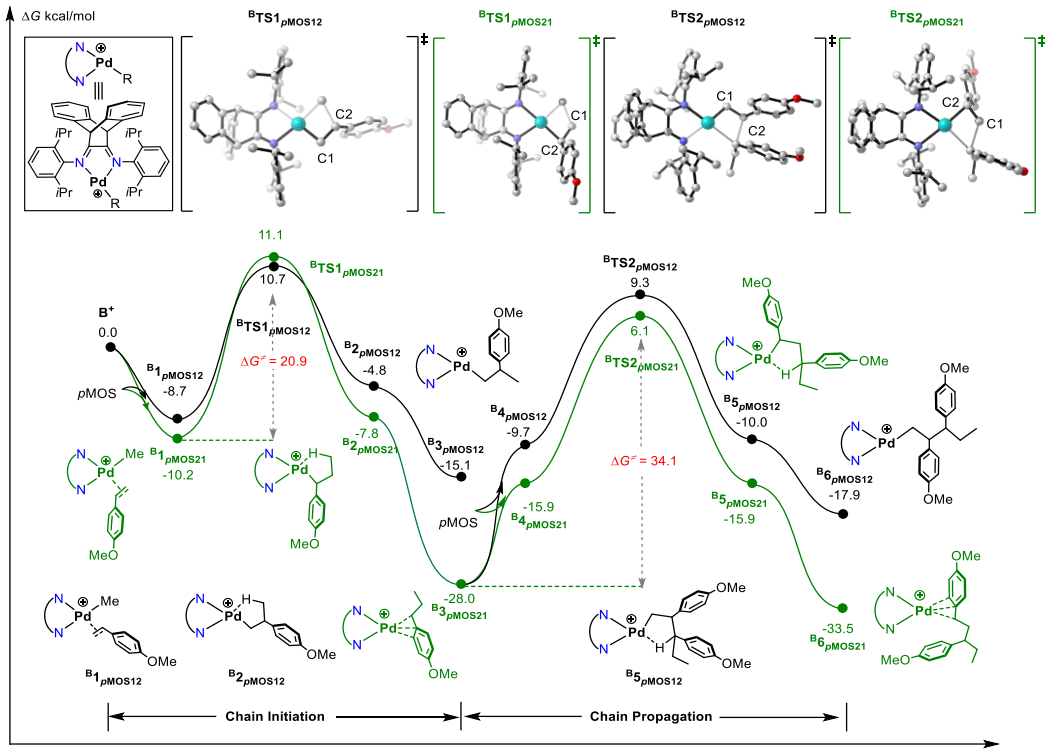

Figure 2. Calculated Gibbs free energy profiles for insertion of *p*MOS based on **B**$^{+}$ at the chain initiation and chain propagation stage (in kcal/mol). The 1,2- and 2,1-insertion pathways are in black and green, respectively.

Given that the two pathways are kinetically competitive and that the 2,1-insertion is thermodynamically more favorable, further calculations were performed on the chain propagation process based on ^{B}**3**$_{p\text{MOS21}}$. These calculations indicated that the 2,1-insertion pathway (^{B}**3**$_{p\text{MOS21}}$→^{B}**4**$_{p\text{MOS21}}$→^{B}**TS2**$_{p\text{MOS21}}$→^{B}**5**$_{p\text{MOS21}}$→^{B}**6**$_{p\text{MOS21}}$) encounters lower energy barriers compared to the 1,2-insertion pathway (^{B}**3**$_{p\text{MOS12}}$→^{B}**4**$_{p\text{MOS12}}$→^{B}**TS2**$_{p\text{MOS12}}$→^{B}**5**$_{p\text{MOS12}}$→^{B}**6**$_{p\text{MOS12}}$), thus making it more advantageous. Nevertheless, the energy barriers for these pathways, at 34.1 and 37.3 kcal/mol, respectively, are prohibitively high, challenging the explanation of catalytic reactivity. This contradiction leads to further analysis that the activation energies for both insertion reactions are similar, with the 1,2-insertion being marginally favored by 0.4 kcal/mol. The Eyring equation further elucidates the relationship between the kinetic constants for the two reactions, k_{12} and k_{21}. Calculated at T=303 K, the ratio k_{12}/k_{21}= exp(($\Delta G_{12}^{\neq}$−$\Delta G_{21}^{\neq}$)/RT) reveals a value of k_{12}/k_{21} = 1.94, suggesting that the 1,2-insertion reaction is kinetically favored. Quantification of the *p*MOS insertion products showed a predominant formation of the 1,2-insertion product ^{B}**3**$_{p\text{MOS12}}$ (66% yield), alongside a lesser amount of the 2,1-insertion product ^{B}**3**$_{p\text{MOS21}}$ (34%). Consequently, the chain propagation process based on ^{B}**3**$_{p\text{MOS12}}$, following the 1,2-insertion, was evaluated. As depicted in Figure 3 (right), the calculations indicate that the 1,2-insertion reaction, proceeding through ^{B}**3**$_{p\text{MOS12}}$→^{B}**4′**$_{p\text{MOS12}}$→^{B}**TS2′**$_{p\text{MOS12}}$→^{B}**5′**$_{p\text{MOS12}}$→^{B}**6′**$_{p\text{MOS12}}$, requires overcoming an energy barrier of only 19.9 kcal/mol, which is lower than that for 2,1-insertion (**^{B}3**$_{p\text{MOS12}}$→^{B}**4′**$_{p\text{MOS21}}$→^{B}**TS2′**$_{p\text{MOS21}}$→^{B}**5′**$_{p\text{MOS21}}$→^{B}**6′**$_{p\text{MOS21}}$**)** by 1.38 kcal/mol. Thus, it is plausible to conclude that for the dibenzobarrelene-based *α*-diimine complex **B**$^{+}$, the chain initiation stage should predominantly follow the 1,2-insertion, potentially a kinetically controlled process.

Preprints.org (www.preprints.org) | NOT PEER-REVIEWED | Posted: 29 October 2024 doi:10.20944/preprints202410.2300.v1

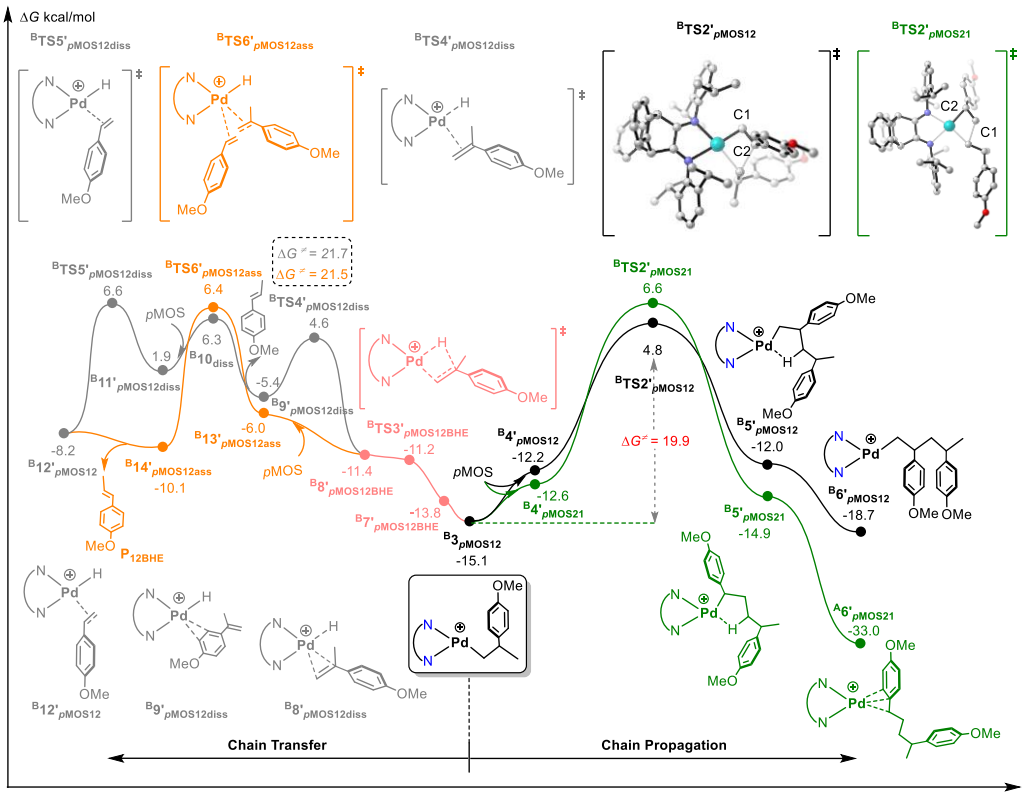

Figure 3. Calculated Gibbs free energy profiles for the $\mathbf{B}^{+}$ mediated competitive pathways for the chain propagation and the chain transfer of *p*MOS based on $^{B}\mathbf{3}_{pMOS12}$ (in kcal/mol). The 1,2- and 2,1-insertion pathways in the chain propagation are in black and green, respectively. The dissociative associative and associative pathways in the chain transfer are in gray and orange, respectively.

To further explore the feasibility of the polymerization reaction, the chain termination process following the chain initiation via 1,2-insertion was examined (Figure 3, left). The chain termination mechanism initiates with *β*−H elimination ($^{B}\mathbf{TS3'}_{pMOS12BHE}$), leading to the intermediate $^{B}\mathbf{8'}_{pMOS12BHE}$ with an activation barrier of 3.9 kcal/mol. Subsequently, two chain transfer pathways were considered: dissociative and associative chain transfer. The dissociative chain transfer pathway proceeds through the Pd−H intermediate $^{B}\mathbf{10}_{diss}$, with an activation barrier of 21.7 kcal/mol (6.6−(-15.1)), and the associative chain transfer, facilitated by *p*MOS via $^{B}\mathbf{TS6'}_{pMOS12ass}$, presents a comparable activation barrier of 21.5 kcal/mol (6.4−(-15.1)). Based on $^{B}\mathbf{3}_{pMOS12}$, chain propagation is kinetically more favorable than the chain transfer processes (19.9 vs. 21.9, 21.4 kcal/mol). This kinetic preference aligns with experimental observations indicating a high 1,2-regioselectivity polymer.

 doi:10.20944/preprints202410.2300.v1

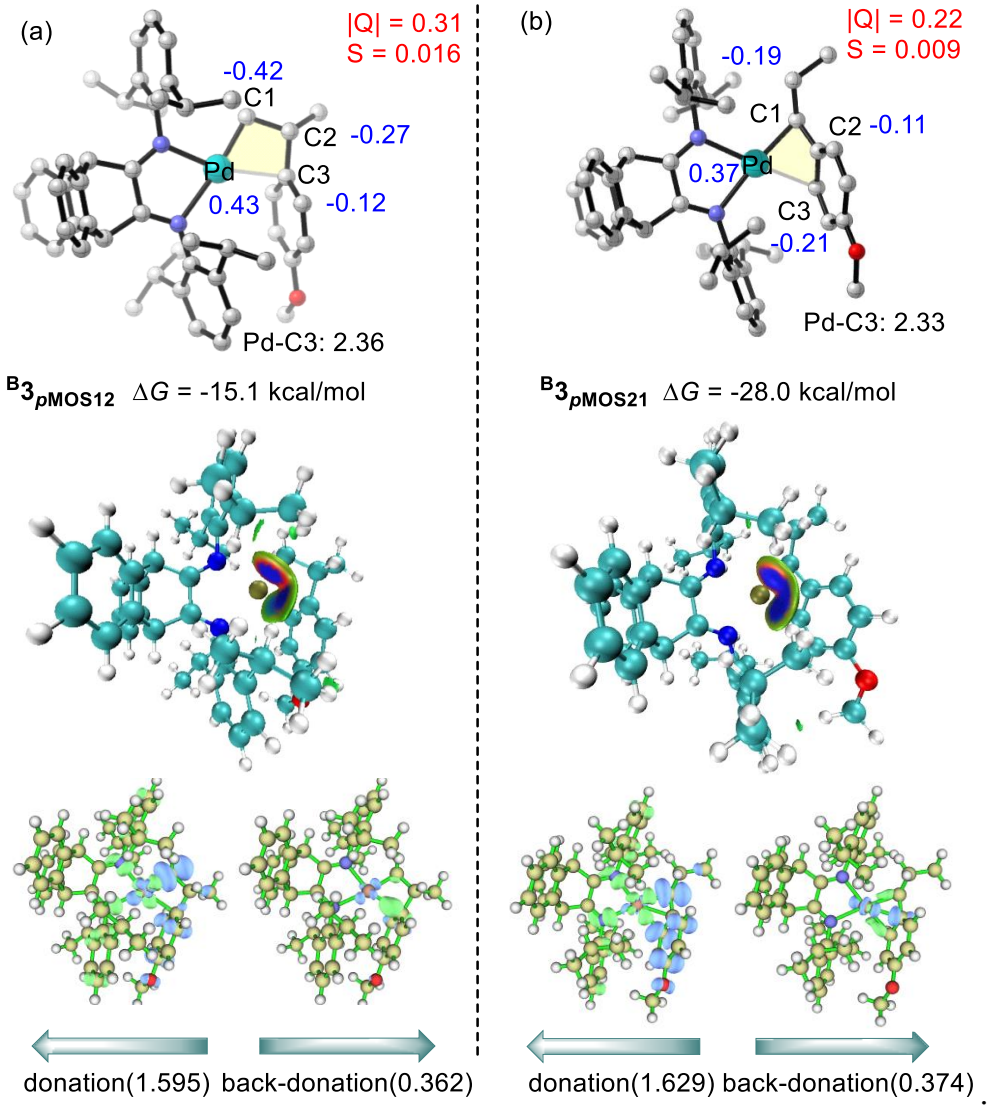

Figure 4. The structures, independent gradient model based on Hirshfeld partition, and Extended Transition State-Natural Orbitals for Chemical Valence analysis for (a) $^{B}3_{pMOS12}$ and (b) $^{B}3_{pMOS21}$ (distances in Å and angles in°).

Comparative analysis revealed that the barrier to chain propagation is significantly large, attributable to the varying thermodynamic stabilities of products from the 1,2- and 2,1-insertion chain initiation modes. Consequently, a detailed examination of $^{B}3_{pMOS12}$ and $^{B}3_{pMOS21}$ is conducted, focusing on their structural characteristics and charge distributions (refer to the top of Figure 4). Charge dispersion is known to contribute to structural stability. In the chain initiation products, the four-membered units comprising Pd, C1, C2, and C3 are critical for chemical reactivity. To assess the stability of these structures, the unsigned average charges ($|Q|$) and square errors (S) of the atoms in intermediates $^{B}3_{pMOS12}$ and $^{B}3_{pMOS21}$ were calculated to estimate charge dispersion. The S value, defined for the Pd, C1, C2, and C3 atoms as $S = \sum(|Q_x| - |Q|)^2/n$, where n = 4 and $|Q|$ represents the unsigned average charge while Q_x denotes the individual atomic charges, serves as an indicator of structural stability. A lower S value indicates higher stability. The average charges for $^{B}3_{pMOS12}$ and $^{B}3_{pMOS21}$ are 0.31 and 0.22, respectively, with S values of 0.016 and 0.009, indicating that $^{B}3_{pMOS21}$ demonstrates a smaller average charge Q and S value compared to $^{B}3_{pMOS12}$, thus suggesting greater thermodynamic stability and a deeper potential well for $^{B}3_{pMOS21}$. Additionally, hirshfeld partition analysis [23,24] demonstrated stronger van der Waals interactions in $^{B}3_{pMOS21}$ (darker blue in the middle of Figure 4) compared to $^{B}3_{pMOS12}$. extended transition state-natural orbitals for chemical valence analysis [23,25] (refer to the bottom of Figure 4) further confirmed stronger donation (1.629 vs 1.595) and back-

 doi:10.20944/preprints202410.2300.v1

donation (0.374 vs 0.362) in $^{B}3_{pMOS21}$ compared to $^{B}3_{pMOS12}$. This analysis supports the identification of η^3-π-benzyl intermediate $^{B}3_{pMOS21}$ as a stable resting state, which impedes further chain propagation.

By comparing the computational results of catalysts **A**$^+$ and **B**$^+$, it is evident that adjusting the steric hindrance of the auxiliary ligand significantly influences the chain initiation insertion mode, thereby affecting activity and regioselectivity. To further explore this effect, a series of complexes with increased steric hindrance was designed and calculated. As illustrated in Figure 5, the isopropyl groups in the N-aryl moieties were replaced with a phenyl group (catalyst **C**$^+$), a methyl-phenyl group (catalyst **D**$^+$), and a phenyl-phenyl group (catalyst **E**$^+$). The computational results of the chain initiation process are summarized in Table 1. These calculations indicate that an increase in the van der Waals volume [26] of the auxiliary ligand leads to a reduced energy barrier gap for 1,2- and 2,1-insertion (ΔΔG (1,2−2,1) changing from 2.8 to -0.4 to 0.2 to -2.4 to -3.3 to -5.2 kcal/mol), making the 1,2-insertion pathway increasingly favorable. A linear relationship was established between ΔΔ*G* (1,2−2,1) and the van der Waals volume of the catalyst (Figure 5), demonstrating a strong negative correlation (R^2 = 0.95). A larger van der Waals volume corresponds to a lower barrier gap ΔΔ*G* (1,2−2,1), which enhances the propensity for 1,2-insertion. This trend suggests that while the barrier for 1,2-insertion is minimally affected by increasing steric hindrance (from 19.5 to 20.9 kcal/mol), the barrier for 2,1-insertion is significantly raised (from 18.0 to 25.0 kcal/mol). Consequently, this alteration leads to a more negative difference in the energy barriers between the two pathways, thereby enhancing the selectivity for 1,2-insertion.

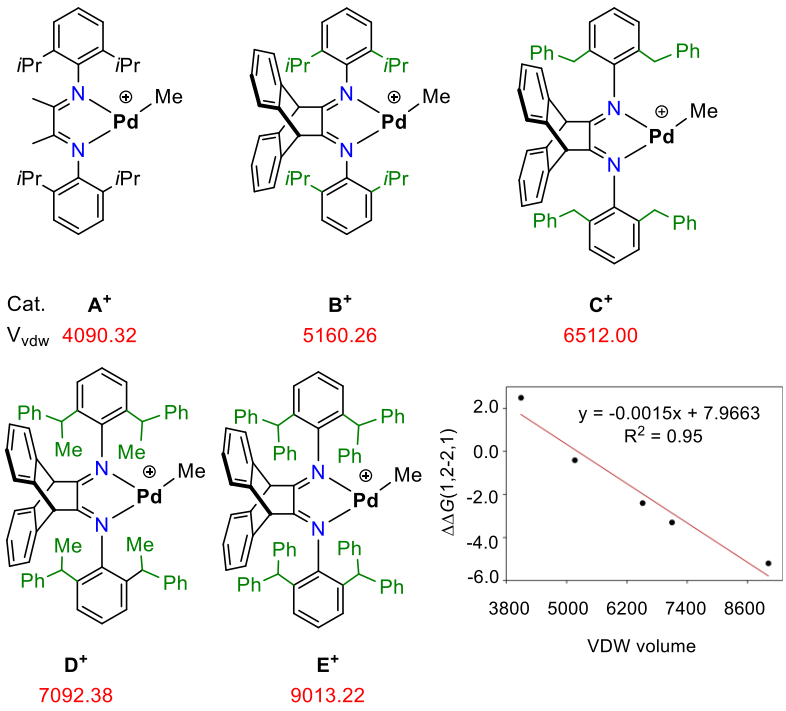

Figure 5. The new designed catalysts, the VDW volumes are given in Bohr^3(red), The R^2 values between the the VDW volume (Bohr^3) of catalysts **A**$^+$, **B**$^+$ or **C**$^+$–**E**$^+$ and their corresponding insertion energy gaps (kcal/mol).

 doi:10.20944/preprints202410.2300.v1

Table 1. Gibbs free energies (kcal/mol) for reactions of *p*MOS insertion for catalysts **A**$^+$, **B**$^+$, and **C**$^+$–**E**$^+$ at the chain initiation stage.

catalysts	$\mathbf{1}_{p\mathrm{MOS21}}$	$\mathbf{TS1}_{p\mathrm{MOS12}}$ ($\mathbf{TS1}_{p\mathrm{MOS21}}$)	$\mathbf{P}_{12}$ ($\mathbf{P}_{21}$)	ΔΔP	Δ*G* (1,2-)	Δ*G* (2,1-)	ΔΔ*G* (1,2−2,1)
A$^+$	-12.5	8.3(5.5)	-17.4(-29.8)	12.4	20.5	18.0	2.5
B$^+$	-10.2	10.7(11.1)	-15.1(-28.0)	12.9	20.9	21.3	-0.4
C$^+$	-15.4	4.5(6.9)	-20.6(-30.5)	9.9	19.9	22.3	-2.4
D$^+$	-6.2	13.3(16.7)	-10.3(-17.1)	6.8	19.5	22.8	-3.3
E$^+$	-8.5	11.3(16.5)	-14.4(-22.8)	8.3	19.8	25.0	-5.2

2.3. Mechanism of Styrene Polymerization by Cationic Species B$^+$

Concurrently, the dibenzobarrelene-based *α*-diimine catalyst **B**$^+$ demonstrates high activity in catalyzing the polymerization of *p*MOS, yet shows no activity in styrene polymerization. This discrepancy prompts an investigation into the factors influencing its activity, which could elucidate the catalyst's regioselectivity for different monomers. Accordingly, the styrene polymerization mechanism using catalyst **B**$^+$ was computationally analyzed (Figure 6). The 2,1-insertion barrier for styrene at the chain initiation stage is calculated to be 18.1 kcal/mol, which is kinetically 1.2 kcal/mol more favorable than the 1,2-insertion. The η^3 intermediate, $^{\mathrm{B}}\mathbf{3}_{\mathrm{St21}}$, formed by 2,1-insertion, is also thermodynamically more stable than the 1,2-insertion product, $^{\mathrm{B}}\mathbf{3}_{\mathrm{St12}}$ (-25.1 vs -13.9 kcal/mol). The ratio of kinetic constants, estimated according to the Eyring equation $k_{12}/k_{21} = \exp((\Delta G_{12}^{\neq} - \Delta G_{21}^{\neq})/RT)$ at T= 303 K, yields a calculated reactivity ratio (k_{12}/k_{21} = 0.14), indicating that 1,2-insertion of styrene into the Pd−Me complex $^{\mathrm{B}}\mathbf{1}_{\mathrm{St21}}$ is less favorable compared to 2,1-insertion. Quantification of the styrene insertion products revealed that 88% yield was of the 2,1-insertion product $^{\mathrm{B}}\mathbf{3}_{\mathrm{St21}}$, with only a trace amount (12%) of the 1,2-insertion product $^{\mathrm{B}}\mathbf{3}_{\mathrm{St12}}$. Thus, subsequent chain propagation is predominantly based on the 2,1-insertion product $^{\mathrm{B}}\mathbf{3}_{\mathrm{St21}}$. Starting from $^{\mathrm{B}}\mathbf{3}_{\mathrm{St21}}$, chain propagation of styrene through the transition state $^{\mathrm{B}}\mathbf{TS2}_{\mathrm{St21}}$ requires overcoming an activation energy of 33.0 kcal/mol. This substantial barrier underscores the challenges in the chain propagation process during styrene polymerization, aligning with experimental observations that no polymers are formed.

 doi:10.20944/preprints202410.2300.v1

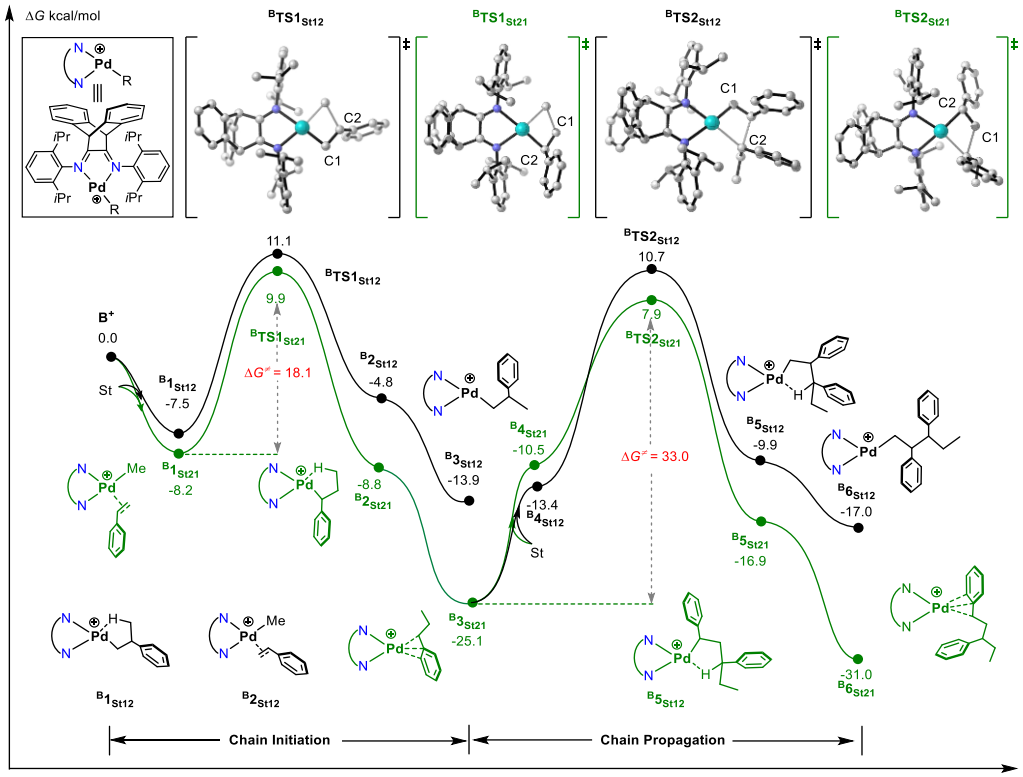

Figure 6. Calculated Gibbs free energy profiles for insertion of styrene based on **B**$^+$ at the chain initiation and chain propagation stage (in kcal/mol). The 1,2- and 2,1- insertion pathways are in black and green, respectively.

3. Computational Details

Theoretical calculations were performed using Gaussian 16. [27] All structures were optimized in the gas phase using the B3LYP-D3 functional [28–30] combined with the Lanl2DZ [31,32] basis set for Pd and the 6-31G(d,p) basis set for other atoms. Polarization functions for Pd were included with ζf = 1.472. [33] Transition states were further verified through intrinsic reaction coordinate (IRC) calculations. [34] Based on the optimized gas-phase geometries, single-point calculations were performed in dichloromethane using the SMD solvent model [35–37] with the B3LYP-D3 functional employing a mixed basis set (SDD for Pd [38,39] and 6-311+G(d,p) for other atoms). Structures in this study were visualized using CYLview. [40] Thermodynamic corrections to Gibbs free energy were applied using solution-phase single-point energies plus 1.9 kcal/mol [41,42] (to adjust for the standard state change from 1 atm to 1 mol/L at 298.15 K), thus calculating the solution-phase Gibbs free energies for subsequent discussions. Tools such as Multiwfn [23] and VMD [43] were utilized to analyze non-covalent interactions (using the independent gradient model based on the Hirshfeld partition method) [24] and to perform extended transition state and natural orbitals for chemical valence analyses [25].

4. Conclusions

DFT studies have analyzed the activity and regioselectivity differences in *para*-alkoxystyrene polymerization catalyzed by cationic *α*-diimine palladium complexes alkyl species [{(2,6-^{i}Pr$_2$C$_6$H$_3$)-N=C(R)-C(R)=N-2,6-^{i}Pr$_2$C$_6$H$_3$)}PdMe]$^+$ (**A**$^+$, R = Me; **B**$^+$, R = dibenzobarrelene) with varying auxiliary ligands. The limited polymer formation observed experimentally with species **A**$^+$ in *para*-methoxystyrene polymerization is attributed to the formation of a stable η^3-benzyl chelate dormant state, resulting from a 2,1-insertion during the chain initiation process. In contrast, species **B**$^+$, demonstrating a high 1,2-regioselectivity in the polymerization process, favors a continuous 1,2-1,2 insertion mode. The 2,1-insertion and 1,2-insertion pathways are dynamically competitive, reflected by similar energy barriers at the chain initiation. The 2,1-insertion intermediate displays enhanced

 doi:10.20944/preprints202410.2300.v1

thermodynamic stability due to a smaller average charge $|Q|$ and square errors S of Pd, C1, C2, and C3 units, thus favoring a dormant state. Conversely, the 1,2-insertion intermediate is more likely to continue coordination and insertion of the subsequent *para*-methoxystyrene monomer. Both dissociative and associative chain transfer pathways have been calculated and considered improbable. Improvements in the catalytic 1,2-regioselectivity of *para*-methoxystyrene polymerization may be achieved by enlarging the substituents on the N-aryl moieties. A series of sterically hindered catalysts were computationally designed to assess the impact of steric effects on the chain initiation step. The results confirm a negative correlation between the energy barrier gap $\Delta\Delta G$ (1,2−2,1) and the van der Waals volume of the catalysts, with a correlation coefficient R^2 of 0.95. A larger van der Waals volume indicates a lower barrier gap $\Delta\Delta G$ (1,2−2,1), which facilitates the occurrence of 1,2-insertion in *para*-methoxystyrene polymerization. Unlike *para*-methoxystyrene polymerization, which is not similarly inhibited and allows subsequent chain propagation, the polymerization of styrene predominantly forms a stable η^3-structured intermediate due to a slightly more favorable 2,1-insertion. These findings are expected to provide valuable insights into the development of cationic α-diimine palladium alkyl species for *para*-alkoxystyrene polymerization.

Supplementary Materials: The following supporting information can be downloaded at the website of this paper posted on Preprints.org, Table S1: Calculated thermodynamic corrections for Gibbs free energies (ΔGcor in Hartrees), solution-phase single-point energies (ΔEsol in Hartrees) and solution-phase Gibbs free energies (ΔGsol in Hartrees). DFT geometries are also collected in a separate .xyz file.

Author Contributions: Conceptualization, L.Z., G.Z. and Y.L.; Methodology, L.Z., G.Z. and Y.L.; Software, X.W.; Formal analysis, X.W.; Investigation, L.Z.; Data curation, L.Z., G.Z. and Y.L.; Writing—original draft, L.Z.; Writing—review & editing, L.Z., X.W., W.Z., G.Z. and Y.L.; Supervision, W.Z., G.Z. and Y.L. All authors have read and agreed to the published version of the manuscript.

Funding: This research was funded by the NSFC (Nos. 22071015) and the Open Funding Project of Key Laboratory of Functional Polymer Materials, Ministry of Education, Nankai University (KLFPM202301).

Data Availability Statement: The original contributions presented in the study are included in the article/Supplementary Materials, further inquiries can be directed to the corresponding author/s.

Conflicts of Interest: The authors declare no conflict of interest.

References

1. Zou, C.; Chen, C. L. Polar-functionalized, crosslinkable, self-healing and photoresponsive polyolefins. *Angew. Chem. Int. Ed*. **2020**, *59*, 395–402.
2. Tan, C.; Zou, C.; Chen, C. Material properties of functional polyethylenes from transition-metal-catalyzed ethylene–polar monomer copolymerization. *Macromolecules* **2022**, *55*, 1910–1922.
3. Mu, H.; Zhou, G.; Hu, X.; Jian, Z. Recent advances in nickel mediated copolymerization of olefin with polar monomers. *Coord. Chem. Rev.* **2021**, *435*, 213802–213818.
4. De, P.; Faust, R. Living carbocationic polymerization of *p*-methoxystyrene using *p*-methoxystyrene hydrochloride/$SnBr_4$ initiating system: determination of the absolute rate constant of propagation for ion pairs. *Macromolecules* **2004**, 37, 7930–7937.
5. Kojima, K.; Sawamoto, M.; Higashimura, T. Living cationic polymerization of *p*-methoxystyrene by the hydrogen iodide/zinc iodide and hydrogen iodide/iodine initiating systems: effects of tetrabutylammonium halides in a polar solvent. *Macromolecules* **1990**, 23, 948–953.
6. Kawamura, T.; Uryu, T.; Matsuzaki, K. Stereoregularity of polystyrene derivatives, 1. poly(methylstyrene)s and poly- (methoxystyrene)s obtained with ziegler catalyst, cationic catalyst, or radical initiators. *Makromol. Chem.* **1982**, 183, 125–141.
7. Iio, K.; Kobayashi, K.; Matsunaga, M. Radical polymerization of allyl alcohol and allyl acetate. *Polym. Adv. Technol.* **2007**, 18 (12),953–958.
8. Chen, M.; Chen, C. L. Direct and tandem routes for the copolymerization of ethylene with polar functionalized internal olefins. *Angew. Chem., Int. Ed.* **2020**, 59, 1206–1210.
9. Mitsushige, Y.; Yasuda, H.; Carrow, B. P.; Ito, S.; Kobayashi, M.; Tayano, T.; Watanabe, Y.; Okuno, Y.; Hayashi, S.; Kuroda, J.; Okumura, Y.; Nozaki, K. Methylene-bridged bisphosphine monoxide ligands for palladium-catalyzed copolymerization of ethylene and polar monomers. *ACS Macro Lett*. **2018**, 7, 305–311.
10. Ota, Y.; Ito, S.; Kobayashi, M.; Kitade, S.; Sakata, K.; Tayano, T.; Nozaki, K. Crystalline isotactic polar polypropylene from the palladium-catalyzed copolymerization of propylene and polar monomers. *Angew. Chem., Int. Ed.* **2016**, 55, 7505–7509.

11. Zhang, Y.; Wang, C.; Mecking, S.; Jian, Z. Ultrahigh branching of main-chain-functionalized polyethylenes by inverted insertion selectivity. *Angew. Chem. Int. Ed.* **2020**, *59*, 14296–14302.
12. Chen, J.; Gao, Y.; Marks, T. J. Early transition metal catalysis for olefin-polar monomer copolymerization. *Angew. Chem., Int. Ed.* **2020**, *59*, 14726–14735.
13. Keyes, A.; Basbug Alhan, H. E.; Ordonez, E.; Ha, U.; Beezer, D. B.; Dau, H.; Liu, Y. S.; Tsogtgerel, E.; Jones, G. R.; Harth, E. Olefins and vinyl polar monomers: bridging the gap for next generation materials. *Angew. Chem., Int. Ed.* **2019**, *58*, 12370–12391.
14. Yuan, S. F.; Yan, Y.; Solan, G. A.; Ma, Y.; Sun, W. H. Recent advancements in N-ligated group 4 molecular catalysts for the (co)polymerization of ethylene. *Coord. Chem. Rev.* **2020**, 411,213254.
15. Wang, Y.; Lai, J.; Gao, R.; Gou, Q.; Li, B.; Zheng, G.; Guo, Z. Recent advances in nickel catalysts with industrial exploitability for copolymerization of ethylene with polar monomers. *Polymers* **2024**, *16*, 1676.
16. Xiao, X.; Zheng, H.; Gao, H.; Cheng, Z.; Feng, C.; Yang, J.; Gao, H. Recent advances in synthesis of non-alternating polyketone generated by copolymerization of carbon monoxide and ethylene. *Int. J. Mol. Sci.* **2024**, 25, 1348
17. Xu, M.; Yu, F.; Li, P.; Xu, G.; Zhang, S.; Wang, F. Enhancing chain initiation efficiency in the cationic allyl-nickel catalyzed (co)polymerization of ethylene and methyl acrylate. *Inorg. Chem.* **2020**, *59*, 4475–4482.
18. Wu, Q.; Wang, W.; Xu, G.; Pang, W.; Li, Y.; Tan, C.; Wang, F. Bulky iminophosphine-based nickel and palladium catalysts bearing 2,6-dibenzhydryl groups for ethylene oligo-/polymerization. *Appl.Organomet. Chem.* **2020**, 34, 5428
19. Guironnet, D.; Roesle, P.; Ru¨nzi, T.; Go¨ttker Schnetmann, I.; Mecking, S. Insertion polymerization of acrylate. *J. Am. Chem. Soc.* **2009**, 131, 422–423.
20. Jian, Z.; Mecking, S. Insertion homo- and copolymerization of diallyl ether. *Angew. Chem. Int. Ed*. **2015**, *54*, 15845–15849.
21. Saki, Z.; D'Auria, I.; Dall'anese, A.; Milani, B.; Pellecchia, C. Copolymerization of ethylene and methyl acrylate by pyridylimino Ni(II) catalysts affording hyperbranched poly(ethylene-co-methyl acrylate)s with tunable structures of the ester groups. *Macromolecules* **2020**, *53*, 9294–9305.
22. Liao, G.; Xiao, Z.; Chen, X.; Du, C.; Zhong, L.; Cheung, C. S.; Gao, H. Fast and regioselective polymerization of *para*-alkoxystyrene by palladium catalysts for precision production of high-molecular weight polystyrene derivatives. *Macromolecules* **2020**, *53*, 256–266.
23. Lu, T.; Chen, Q. Independent gradient model based on hirshfeld partition: a new method for visual study of interactions in chemical systems. *J. Comput. Chem.* **2022**, *43*, 539–555.
24. Lu, T.; Chen, F. Multiwfn: a multifunctional wavefunction analyzer. *J. Comput. Chem.* **2012**, *33*, 580–592.
25. Mitoraj, M. P.; Michalak, A.; Ziegler, T. A combined charge and energy decomposition scheme for bond analysis. *J. Chem.Theory Comput.* **2009**, 5, 962–975.
26. Bondi, A. Van der waals volumes and radii. *J. Phys. Chem.* **1964**, 68, 441–451.
27. Frisch, M. J.; Trucks, G. W.; Schlegel, H. B.; Scuseria, G. E.; Robb, M. A.; Cheeseman, J. R.; Scalmani, G.; Barone, V.; Petersson, G. A.; Nakatsuji, H.; et al. *Gaussian 16, Revision A.03*; Gaussian, Inc.: Wallingford, CT, USA, **2016**.
28. Lee, C.; Yang, W.; Parr, R. G. Development of the colle salvetti correlation-energy formula into a functional of the electron density. *Phys. Rev. B Condens. Matter Mater. Phys*. **1988**, *37*, 785–789.
29. Grimme, S.; Antony, J.; Ehrlich, S.; Krieg, H. A Consistent and accurate Ab initio parametrization of density functional dispersion correction (DFT-D) for the 94 elements H–Pu. *J. Chem. Phys*. **2010**, 132, 154104.
30. Huang, W.; Xi, Y.; Pan, D.; Fan, L.; Fang, K.; Huang, G.; Chen, Y. Palladium-catalyzed enantioselective multicomponent cross-coupling of trisubstituted olefins. *Journal of the American Chemical Society* **2024,** 146, 16892–16901.
31. Hay, P. J.; Wadt, W. R. Ab initio effective core potentials for molecular calculations. potentials for the transition metal atoms Sc to Hg. *J. Chem. Phys.* **1985**, *82*, 270–283.
32. Uchikura, T.; Kato, S.; Makino, Y.; Fujikawa, M. J.; Yamanaka, M.; Akiyama, T. Chiral phosphoric acid-palladium(II) complex catalyzed asymmetric desymmetrization of biaryl compounds by C(sp^3)-H activation. *J. Am. Chem. Soc.* **2023**, 145, 15906–15911.
33. Ehlers, A. W.; Böhme, M.; Dapprich, S.; Gobbi, A.; Höllwarth, A.; Jonas, V.; Köhler, K. F.; Stegmann, R.; Veldkamp, A.; Frenking, G. A set of f-polarization functions for pseudo-potential basis sets of the transition metals Sc-Cu, Y-Ag and La-Au. *Chem. Phys. Lett.* **1993**, *208*, 111–114.
34. Fukui, K. The path of chemical reactions-the IRC approach. *Acc. Chem. Res.* **1981**, *14*, 363–368.
35. Marenich, A. V.; Cramer, C. J.; Truhlar, D. G. Universal solvation model based on solute electron density and on a continuum model of the solvent defined by the bulk dielectric constant and atomic surface tensions. *J. Phys. Chem. B.* **2009**, *113*, 6378–6396.
36. Ni, H. Q.; Karunananda, M. K.; Zeng, T.; Yang, S.; Liu, Z.; Houk, K. N.; Liu, P.; Engle, K. M. Redox-paired alkene difunctionalization enables skeletally divergent synthesis. *J. Am.Chem. Soc.* **2023**, 145, 12351–12359.

 doi:10.20944/preprints202410.2300.v1

37. Ni, H. Q.; Alturaifi, T. M.; Rodphon, W.; Scherschel, N. F.; Yang, S.; Wang, F.; Engle, K. M. Anti-selective cyclopropanation of nonconjugated alkenes with diverse pronucleophiles via directed nucleopalladation. *Journal of the American Chemical Society* **2024**,*146*, 24503–24514.
38. Andrae, D.; Haüβermann, U.; Dolg, M.; Stoll, H.; Preuβ, H. Energy-adjusted ab initio pseudopotentials for the 2nd and 3rd row transition-elements. *Theor. Chim. Acta.* **1990**, *77*, 123–141.
39. Zhang, P.; Guo, C. Q.; Yao, W.; Lu, C. J.; Li, Y. Z.; Paton, R. S.; Liu, R. R. Pd-catalyzed asymmetric amination of enamines: expedient synthesis of structurally diverse N-C atropisomers. *ACS Catal.* **2023**, 13, 7680–7690.
40. Legault, C.Y. *CYLView, Version 1.0b*; Université de Sherbrooke: Sherbrooke, Quebec, Canada, **2020**. Available online: http://www.cylview.org (accessed on 11 April , 2023).
41. Liu, C.; Qin, Z. X.; Ji, C. L.; Hong, X.; Szostak, M. Highly-chemoselective step-down reduction of carboxylic acids to aromatic hydrocarbons via palladium catalysis. *Chem. Sci.* **2019**, *10*, 5736–5742.
42. Fan, H.; Kang, X.; Dai, S. Stable ultrahighly branched polyethylene synthesis via externally robust chain-walking polymerization. *ACS Catal.* **2024**, 14, 13531−13541.
43. Humphrey, W.; Dalke, A.; Schulten, K. VMD: Visual molecular dynamics. *J. Mol. Graph.* **1996**, *14*, 33–38.